Gold Nanorod Coating with Silica Shells Having Controlled Thickness and Oriented Porosity: Tailoring the Shells for Biosensing

Vincent Pellas, Juliette Blanchard, Clément Guibert, Jean-Marc Krafft, Antoine Miche, Michèle Salmain, Souhir Boujday

Gold Nanorods Coating with Silica Shells Having Controlled Thickness and Oriented Porosity: Tailoring the Shells for Specific Applications

Vincent Pellas[1,2], Juliette Blanchard[1,*], Clément Guibert[1], Jean-Marc Krafft[1], Antoine Miche[1], Michèle Salmain[2,*], Souhir Boujday[1,*]

[1] Sorbonne Université, CNRS, Laboratoire de Réactivité de Surface (LRS), 4 place Jussieu, F-75005 Paris, France.

[2] Sorbonne Université, CNRS, Institut Parisien de Chimie Moléculaire (IPCM), 4 place Jussieu F-75005 Paris, France.

KEYWORDS: Gold nanorods, silica coating, core-shell, porosity, colloidal stability, purification.

ABSTRACT:

The coating of gold nanorods with a silica shell (AuNR@SiO_2) is an effective way to extend their use in a wide variety of biomedical applications. A silica shell offers numerous advantages as it provides more stability, frees the surface from toxic cetyltrimethylammonium bromide (CTAB), and preserves the rod shape under photothermal conditions. We introduce herein a new strategy to perform this coating based on dissociation of tetraethylorthosilicate (TEOS) hydrolysis and condensation reactions. This dissociation is achieved by a pH modulation of the reaction medium, and, depending on selected pH conditions, AuNR@SiO_2 with thick silica shell having an organized mesoporosity aligned either parallel (AuNR@//m-SiO_2) or perpendicular (AuNR@⊥m-SiO_2) to the AuNR surface were generated. Moreover, when mercaptopropyltrimethoxysilane (MPTMS) was used as a surface primer prior to TEOS condensation, ultrathin and homogeneous silica shells (AuNR@t-SiO_2) of controllable thickness in the range 2-6 nm, are produced. These protocols proved robust enough to prevent contamination with core-free silica particles. While formation, at high TEOS concentration of these nanoparticles, is evidenced by TEM analysis before the purification procedure, their total elimination during the purification step was achieved by addition of a suitable amount of CTAB to ensure the colloidal stability of the core-free and core-shell nanoparticles. Complete elimination of CTAB was demonstrated by SERS when ligand exchange of CTAB by MPTMS is first carried out. In a preliminary study, AuNR@t-SiO_2 particles were used to build up a nanoprobe aimed at the label-free plasmonic immunodetection of a model target in solution.

Introduction

Gold nanorods (AuNRs) are now, and over several decades, established as central items for biological applications. Their ability to absorb light upon irradiation originates from the collective oscillation of electrons in the conduction band of the gold surface; it results in two localized Surface Plasmon Resonance (LSPR) bands called the transversal and longitudinal bands, t-LSPR and l-LSPR, respectively; they correspond to the resonance along the short and long axes of the particle, respectively.[1,2] The position of l-LSPR band can be finely tuned from 600 and up to 1800 nm by controlling the particle aspect ratio.[3,4] This versatility is of high interest for biomedical applications such as photothermal therapy because of the minimal absorption of blood and human tissues in this region.[5] Moreover, the position of l-LSPR band displays a higher sensitivity to the variation of the local dielectric environment compared to the LSPR band of spherical nanoparticles, making AuNRs of particular interest for the development of LSPR biosensors.[6–9] The extensive development of synthesis protocols enables the preparation of particles with desired and controlled properties, mainly using cetyltrimethylammonium bromide (CTAB) as surfactant, surface stabilizer, and shape inducing agent.[10] However, the cytotoxicity of CTAB and its interferences with biological processes, restrict the biomedical applications of AuNRs.[11–16] Besides the damaging effect of CTAB, AuNRs are not stable under irradiation and reshape into spherical nanoparticles[17]. To overcome these limitations, the growth of a silica shell on AuNRs, also referred as silica coating, is the most promising route and has expanded tremendously over the last decade as it allows to eliminate or screen CTAB while preserving AuNRs' shape and therefore, their optical properties. Few materials are as universal and versatile as silica in terms of porosity, controlled thickness and surface modification.[18] Silica coating of AuNRs to generate core-shell particles (AuNR@SiO_2) has proven to reduce aggregation and toxicity,[16,19,20] enhance the thermal stability,[21–23] the photoacoustic signal[24] *via* faster heat transfer to the environment[25], and provide a convenient surface for subsequent functionalization [9,26,27].

Depending on the desired application, the specifications for the silica shell can be radically different. Indeed, the growth, on AuNRs, of a thick mesoporous porous shell (AuNR@m-SiO_2) is preferred for drug delivery applications as it enables drug encapsulation within the pores and its release through light irradiation of the gold core.[28] On the other hand, for applications such as LSPR biosensing, the proximity of the bioreceptor to the gold core is mandatory,[29,30] therefore a thin homogeneous layer is required to maintain the ability of AuNR@SiO_2 to transduce binding events.[9]

Over the last decades, several methods were reported for AuNRs coating with silica. The Stöber process, initially used to synthesize monodisperse silica spheres *via* a base-catalyzed hydrolysis and condensation of tetraethylorthosilicate (TEOS), provides the basis for silica coating on inorganic nanoparticles.[31] Gorelikov and Matsuura were the first to adapt this procedure to directly coat CTAB-stabilized AuNRs with a mesoporous silica shell.[32] Since then, numerous articles have been published on the coating of AuNRs with silica either directly,[33–38] or using a surface primer such 3-aminopropyltrimethoxysilane (APTMS),[39] 3-mercaptopropyltrimethoxysilane (MPTMS),[40–42] O-*[*2-*(*3-Mercaptopropionylamino*)*ethyl*]*-O′-methylpolyethylene glycol (mPEG-SH)[43] or polyelectrolyte layers[44] prior to silica shell formation. We have recently surveyed the variety of synthetic methods that have been developed to encapsulate AuNRs with silica shell and discussed the multiple issues left to overcome. Among other issues, further improvements of the coating protocols are still needed to master the shell homogeneity, precisely predict its thickness, control its porosity, and avoid

contamination of the samples with core-free silica NPs formed by homogeneous nucleation of silica.[9] We have therefore undertaken to set up simple and robust methods to coat AuNRs with silica, as part of our endeavors to develop LSPR biosensors.

In what follows, we report new protocols intended to control both pore organization and shell thickness of silica-coated gold nanorods (AuNR@SiO_2) based on a pH modulation of the reaction medium during the coating step. In fact, all the previously published papers dealing with the coating of AuNRs with silica were based on the simultaneous hydrolysis and condensation of TEOS that both quickly occur at high basic pH (pH range 10-11). Our approach rather relies on the fact that the pH of the reaction medium determines the rates of the two sol-gel reactions responsible for deposition of SiO_2, that is TEOS hydrolysis and condensation. In acidic conditions, the kinetics of TEOS condensation reaction is slow, while it is fast under basic conditions.[45] We show here, for the first time, the impact of a kinetically-controlled condensation of silica on shell formation and on pores organization. Different Au/TEOS ratios were investigated and the in-depth analysis at each step of the synthesis, including before purification, allowed us to analyze the coating process and master its dependency to the pH. This approach was applied to the production of AuNR@SiO_2 with controlled thicknesses and porosities. In the protocols developed herein, mesoporous silica shells, with a thickness tunable in the range 13 to 21 nm were successfully produced, and, depending on the pH conditions, we can direct the orientation of the silica porosity to be either perpendicular to the AuNR surface (AuNR@⊥m-SiO_2) or, for the first time, to the best of our knowledge, parallel to the surface (AuNR@//m-SiO_2). With the same approach we also synthesized ultrathin silica shells (AuNR@t-SiO_2) of tunable thickness in the range from 2 to 6 nm, using MPTMS as a surface primer prior to TEOS condensation. The mechanisms of silica growth are well-investigated here relying on a very large set of characterization techniques and allow us to precisely discuss several aspects among which the fate of CTAB and homogeneous nucleation of silica nanoparticles. We believe that through the protocols optimized in this work, the specification sheet for the silica shell can be fulfilled whatever the intended application of the final AuNR@SiO_2 nanomaterials.

EXPERIMENTAL SECTION

Materials: Hydrogen tetrachloroaurate (III) trihydrate (≥99.99%; $HAuCl_4 \cdot 3H_2O$) was purchased from Alfa Aesar. Sodium borohydride (98%; $NaBH_4$), Sodium hydroxide (NaOH), Cetyltrimethylammonium bromide (BioUltra ≥99.0%; CTAB), (3-Mercaptopropyl) trimethoxysilane (95%; MPTMS), Tetraethyl orthosilicate (≥99.0%; TEOS) were purchased from Sigma-Aldrich. Silver nitrate (≥99%; $AgNO_3$), Ascorbic acid (≥99.0%) were purchased from Honeywell, Fluka. Sodium oleate (≥97.0%; NaOL) was purchased from TCI Chemicals. Hydrochloric acid (37%; HCl) was purchased from VWR chemicals. Millipore ultrapure water (18.2 MΩ cm) was used throughout the experiments. For the experiments performed at room temperature, the value in our experimental room is 20 ± 2°C.

Gold nanorods synthesis: AuNRs were synthesized following a seed-mediated growth method using a binary surfactant system, a protocol that has proved to lead to monodisperse AuNRs with negligible shape impurities.[46] Briefly, the seed solution was prepared by mixing 5 mL of 0.50 mM $HAuCl_4 \cdot 3H_2O$ with 5 mL of 0.2 M CTAB aqueous solutions. Then, 0.6 mL of freshly prepared ice cold 10 mM $NaBH_4$ solution was diluted to 1.0 mL with water and then injected to the Au^{III} – CTAB solution under vigorous stirring (1000 rpm) for 2 min to form the gold

seeds. The seed solution was matured at 30 °C for 30 min before use. The growth solution was then prepared by dissolving 9 g of CTAB (~ 99 mM) and 1.234 g of NaOL (~16 mM) in 250 mL of water at 50 °C. This solution was allowed to cool down to 30 °C and then 18 mL of a 4 mM $AgNO_3$ solution were added and the resulting solution was kept without stirring for 15 min at 30 °C. Then, 250 mL of 1 mM pre-heated (30 °C) $HAuCl_4 \cdot 3H_2O$ aqueous solution was introduced into the above solution and allowed to react for 90 min at 700 rpm. Next, 1.5 mL of HCl 37 wt % was added to lower the pH to 1.5 and stirring was maintained at 400 rpm for another 15 min. 1.25 mL of a 64 mM ascorbic acid aqueous solution was added afterwards, and the solution was briefly stirred for 30 s. Finally, 50 μL of the seed suspension were injected under vigorous stirring (1000 rpm) in 30 s to initiate the growth. The resulting suspension was then aged undisturbed overnight (12 h) at 30 °C. It was centrifuged the next day at 5600 rcf (relative centrifugal force) for 20 min to remove the excess reactants. The obtained AuNRs were collected (~ 4.2 mL after centrifugation) and sonicated in an ultrasonic bath (50-60 kHz, 90 W) until complete redispersion (10-20 min). AuNRs were diluted to 20 mL with pure water [CTAB] ~ 10 mM) and stored at 30 °C. Multiple syntheses of AuNRs have been carried out for this study (20 mL per batch). As previously reported,[7] the AuNRs from these batches differ slightly, although the exact same protocol has been followed, (see Figure S 1 for TEM and UV-Vis absorption spectra and Figure S 2 for morphological distribution, DLS and zeta potential, in SI). Extended description regarding the synthesis and characterization of the obtained AuNRs is also provided in SI.

The yield of gold salt reduction to metallic gold was estimated to ca. 65 % by monitoring the absorbance intensity of AuNRs "raw" solutions at 400 nm (see the part of the experimental section dealing with the analysis of the UV-Vis spectra). Hence, metallic gold concentration was evaluated to $[Au^0] \approx 8.1$ mM. Based on this concentration in reduced gold and assuming that no AuNRs were lost during the centrifugation steps, it is possible to estimate the molar concentration of AuNRs using a rough estimation of the mean volume of a particle (considered as a cylinder ended with two half spheres) and the average dimensions of the AuNRs obtained from the analysis of the TEM micrographs. This estimated concentration is [AuNR] ≈1.0 nM for AuNR. This value is given as an indication and we will refer to the reduced gold concentration as this value remains constant regardless of the batch of AuNRs.

Silica shell growth on gold nanorods (AuNR@SiO_2): Prior to SiO_2 coating, 3.8 mL of the obtained AuNRs were concentrated to 500 μL by centrifugation (5600 rcf; 15 min) and then diluted to a final volume of 5 mL with pure water to adjust the CTAB and Au^0 concentrations respectively to 1.1 mM and 6.2 mM (i.e. [AuNR] = 0.8 nM). Then the pH of the suspensions (depending on the synthesis 3.5 to 4.5) was adjusted to 4.0 by adding small amounts of 0.1 M NaOH or HCl solution using micropipette, these suspensions were stirred for 20 min at 400 rpm. Several protocols were used for silica shell growth as described below.

Protocol A*, Coating at pH 4 without primer:* 125 μL of 20 % TEOS in MeOH (*i.e.* final Au/TEOS molar ratio 1/3.6) were added to 5 mL of the above-described aqueous suspension of AuNRs, then the suspension was stirred 20 min at 400 rpm and kept for 1 -19 days at room temperature without stirring. The resulting core-shell NPs are referred to as *(AuNR@//m-SiO_2).*

Protocol B*, Synthesis with pH-swing and without primer:* A volume x of 20 % TEOS in MeOH (where x = 31, 62 or 124 μL for a final Au/TEOS mole ratio of 1/0.9, 1/1.8 or 1/3.6, respectively) was added to 5 mL of an aqueous suspension of AuNRs (CTAB concentration: either 1.1 or 1.6 mM) and the solution was stirred 1 h at 800 rpm. Initial gold concentration and initial pH were kept at 6.2 mM and pH = 4, respectively. Then, the pH was increased to 8 by

adding 0.1 M NaOH, the solution was stirred for 20 min at 400 rpm and then kept for 20 h at room temperature without stirring. The pH change was done by injecting 0.1 M NaOH with a syringe pump at a constant flow rate of 5 µL/min until reaching pH 8.0. The resulting core-shell NPs are referred to as *(AuNR@⊥m-SiO_2).*

***Protocol C**, synthesis with pH-swing and with primer*: 41 µL of 100 mM MPTMS solution in EtOH were added to 5 mL aqueous solution of AuNRs at pH = 4 and with CTAB concentration of 1.6 mM, and the solution was stirred 3 h at 400 rpm. Then, a volume x of 20 % TEOS in MeOH (where x = 31, 62 or 124 µL for a final Au/TEOS mole ratio of 1/0.9, 1/1.8 or 1/3.6, respectively), was added and the suspension was stirred 1 h at 800 rpm. The pH was then increased by injecting 0.1 M NaOH with a syringe pump at a constant flow rate of 5 µL/min until reaching pH 8.0. The suspension was then stirred for 20 min at 400 rpm and kept afterwards for 20 h at room temperature without stirring. The resulting core-shells NPs are referred to as *(AuNR@t-SiO_2)*

Purification: The day after synthesis, the solutions were sonicated then centrifuged at 7060 rcf for 15 min at room temperature. The supernatant was removed, leaving a minimum of liquid in the centrifuge tube; then the sedimented particles were redispersed four times with 25 mL of EtOH and twice with 25 mL of water; particles were collected by centrifugation after each of these redispersions. After the last cycle, the purified core-shell nanostructures were dispersed in 5 mL of water.

***Nanoimmunoprobe synthesis**:* Affinity-purified goat anti-rabbit Antibody (Ab) (12 µg/mL final concentration) was added to a suspension of AuNR@t-SiO_2 in 5 mM phosphate pH 7.4 (1.5 ml; Optical Density at λmax, $OD_{\lambda max}$ ~ 0.6). The solution was stirred for 90 min at RT and solid BSA was added to a final concentration of 0.5% (w/v). The suspension was stirred for another 45 min and submitted to 4 cycles of centrifugation at 9000 rpm for 10 min and dilution with 5 mM phosphate pH 7.4 containing 0.25% BSA (w/v).

***LSPR biosensing of rabbit IgG**:* AuNR@t-SiO_2-Ab in 5 mM phosphate pH 7.4, 0.25% BSA (0.4 ml; OD_{lmax} ~ 0.9) was dispensed in a plastic cuvette and the target, a rabbit IgG, was added at a concentration of 500 ng/mL. The extinction spectrum of the mixture was measured after 1 h. A negative control experiment was performed by replacing the specific target, rabbit IgG, by mouse IgG (non specific target).

UV-Vis Spectroscopy. UV-Visible (UV-Vis) extinction spectra were recorded on a Cary 50 spectrophotometer (Varian, Inc.) and the analysis of colloidal dispersions was performed in the range 400–1100 nm using a cuvette with 1 cm optical path length. Water was used as the blank. According to refs.[47,48] the OD_{400} linearly correlates with the Au^0 concentration and an absorbance of 1.2 at 400 nm corresponds to 100 % reduction of a 0.5 mM gold salt solution. According to this relation, the reduction yield of Au^{3+} was estimated.

Dynamic light scattering (DLS) and Electrophoretic Light Scattering (ELS). DLS and ELS measurements were performed using a Litesizer™ 500 apparatus (Anton Paar) equipped with a 658 nm laser operating at 40 mW. The scattered light collection angle was set to 90°. The zeta potential (ELS) was measured in a Ω-shaped capillary tube cuvette with an applied potential of 150 V.

Electron microscopy. TEM images of AuNRs and AuNR@SiO_2 were obtained using a JEOL JEM 1011 transmission electron microscope (TEM) operating at an accelerating voltage of

100 kV. The samples were prepared by depositing a drop of water-diluted (x 20) particle suspension onto a carbon-coated copper grid and drying the grid at room temperature before imaging. The size distribution of AuNRs and the silica shell thickness of AuNR@SiO_2 was established by counting a minimum of 200 particles and 200 shells by TEM using Image J Software.

SEM. Scanning electron microscopy images were obtained using a SEM-FEG Hitachi SU-70 scanning electron microscope (Hitachi High-Technologies Corporation, Tokyo, Japan) with an accelerating voltage of 5 kV; the working distance is around 3.5 mm; in lense secondary electron detector SE(U) was used. The samples were prepared by depositing a drop of water-diluted (x 20) particle suspension on an alumina SEM support with a carbon adhesive tape without being coated.

SERS. Surface Enhanced Raman Scattering spectra were recorded in the 100 - 3450 cm^{-1} range on a modular Raman spectrometer (Model RXN1, Kaiser Optical Systems, Inc.). It includes a high-powered near-IR laser diode working at 785 nm and a 1024×256 pixels CCD detector showing a 4 cm^{-1} resolution. Spectra were collected on 1.5 mL of undiluted colloidal suspension in a quartz cuvette. The laser output power was 300 mW. For each spectrum, 10 acquisitions of 90 s were recorded to improve the signal-to-noise ratio.

XPS. X-Ray photoelectron spectrometry analyses were performed using a Scienta Omicron Argus X-ray photoelectron spectrometer equipped with an Al Kα monochromatic radiation source (hν = 1486.6 eV) operating at 280 W power. The analysis is performed under Ultra High Vacuum (≤ 10-9 mBar). The photoelectrons are analyzed in a direction making an angle of 45° to the surface. The spectra were performed with a passing energy of 100 eV for the general spectrum and 20 eV for the N 1s regions. Spectrum analysis were performed using Casa XPS v.2.3.15 software (Casa Software Ltd, U.K.). 1.5 mL of the purified colloidal suspensions of AuNR@//m-SiO_2; AuNR@⊥m-SiO_2 and AuNR@t-SiO_2 were concentrated by centrifugation (10 min at 9000 rpm) to a volume of 30 μL. The resulting suspensions were then deposited as 10 μL drops on indium substrates and dried in air for 2 h before analysis.

RESULTS AND DISCUSSION

Gold nanorods synthesis and characterization: The AuNRs used in this study were synthesized following a seed-growth process. Several batches were prepared to assess the reproducibility of the synthesis and characterized by TEM, UV-Vis spectroscopy, DLS and zeta potential measurements (Figures S1 and S2). Despite some changes in both width and length from batch to batch, the resulting l-LSPR bands were always located around 750 nm and the AR was close to 2.6 (Figure S1). A more detailed discussion on the reproducibility of the synthesis is given in SI section. AuNRs were also characterized by DLS and zeta potential measurements (Figure S2). DLS measurements evidence a colloidal stability and a positive zeta potential (+47 mV) was measured, consistently with the presence of the charged head groups of the CTAB bilayer on the particle surface. Finally, AuNRs were analyzed by SERS (Figure S3). The spectra were dominated by CTAB bands (see table S1 for a detailed assignment of Raman bands).

Silica growth on gold nanorods: silica formation mechanism is governed by the reactions of hydrolysis and condensation of alkoxysilane (Figure S4). These two reactions are catalyzed at

acidic and basic pH (Figure S5), while most existing protocols stipulate strictly basic conditions (pH=10-11).[32,34,36,38] At these high-pH conditions, both hydrolysis and condensation reactions of the alkoxysilane take place simultaneously with fast kinetics. However, by tuning the pH values, it is possible to separate these two reactions and achieve a better control of silica shell growth around AuNRs. These conditions were explored in the three protocols developed herein and are depicted precisely in Scheme 1. These three protocols are labeled A, B, and C and lead to samples referenced AuNR@//m-SiO_2, AuNR@⊥m-SiO_2, and AuNR@t-SiO_2, respectively.

Scheme 1: Pathways adopted for the three protocols developed to grow a silica shell on A*uNRs, A, B, and C for AuNR@//m-SiO_2, AuNR@⊥m-SiO_2, and AuNR@t-SiO_2, respectively.*

Silica growth on gold nanorods following Protocol A, AuNR@//m-SiO_2: In Protocol A, the coating reaction was performed without a primer at pH 4 (Scheme 1), a pH at which the condensation kinetics is significantly slowed down, while the hydrolysis rate is fast (Figure S 5). Moreover, we used a high TEOS concentration (*i.e.* final Au/TEOS mole ratio 1/3.6) and a CTAB concentration of 1.1 mM. The CTAB-capped AuNRs used for this study have average dimensions of 102 × 40 nm (AR = 2.6). The morphology of the silica shell *vs.* the time of reaction was monitored through the analysis of TEM micrographs from samples obtained at different reaction times (Figure 1). Images of the obtained core-shell materials (Figure 1-a, b, c) show a progressive thickening and an improved shell organization when reaction time increases. The mesoporosity of the silica shell is clearly observable and oriented parallel to gold core, hence the AuNR@//m-SiO_2 designation. At day 2, the silica shell only partially covers the gold cores. This partial coating is not sufficient to maintain the colloidal stability of the core-shell nanoparticles as we did observe the aggregation of the particles upon their washing in ethanol (the color due to the plasmonic bands disappears). At day 5, the colloidal stability is improved after washing. However, the silica shell order and homogeneity seem still poor (Figure 1-a). A higher organization is observed starting from day 13 (Figure 1-b, and Figure S 6-a for high resolution large size images). Indeed, TEM micrographs show an ordered silica shell with a thickness of approx. 13.5 (± 5.3) nm displaying an "onion shaped" porosity. At day 17, the thickness of the silica shell is not significantly increased but additional protrusions of approx. 6.0 nm can be observed (Figure 1-c and e). Similar protrusions were reported by Wang et al. and assigned to an important depletion of CTAB and silicate in solution.[49]

Figure 1: Results for protocol A, AuNR@//m-SiO_2: a, b, and c, TEM images taken at different reaction times: 5, 13, and 17 days, respectively. Scale bar in the insert corresponds to 100 nm. (d) Extinction spectra of the original AuNRs and AuNR@//m-SiO_2 before and after washing for 17 days reaction time. (e) SEM images for (c).

The extent of the reaction was also monitored by measuring the extinction spectrum of the crude AuNR@//m-SiO_2 sample (Figure 1-d and Figure S 6-b). Negligible displacement of the l-LSPR band during the first two days confirms the slow kinetics of silica condensation around the AuNRs in these conditions. A red-shift of the l-LSPR band from 742 nm (day 1) to 758 nm (day 17) is observed (Figure 1-d) that can be attributed to a higher refractive index at the AuNR surface upon formation of a silica shell whose thickness increases upon aging.[42,50] The l-LSPR band position seems to stabilize around day 13. DLS measurements shown in Figure S6-c confirm the colloidal stability. After purification, a large blue shift of the LSPR band from 758 nm to 738 nm is observed (Figure 1-d) possibly due to the removal of CTAB. Indeed, zeta potential measurements recorded before purification of AuNR@//m-SiO_2 show a positive value (+32 mV) indicating the presence of CTAB molecules adsorbed on top of the silica layer (Figure S6-d). Once purified, the zeta potential of AuNR@//m-SiO_2 becomes negative, -30 mV, consistently with silica surface charge and CTAB removal (Figure S6-d). CTAB removal was

further confirmed by SERS (Figure S3 and Table S1). SERS data show a drastic decrease in CTAB signal corroborating the previous assumptions. Finally, XPS analysis was performed to check the presence of residual nitrogen atoms due from the ammonium groups of CTAB, and here again, the obtained spectrum (Figure S7-a) evidences the absence of nitrogen and further confirms the successful removal of CTAB allowing for the use of these nano-objects within body fluids without suffering from CTAB toxicity.

To better understand the mechanism of silica growth, we undertook to calculate the amount of TEOS involved in the shell growth. Prior to our calculations, we performed a TEM analysis before purification of the core-shell AuNR@//m-SiO_2 NPs to see whether TEOS also led to a homogeneous nucleation of silica nanoparticles. The images in Figure S 6-e and f clearly show that almost no core-free silica particles were formed. ~~Consequently, the amount of TEOS consumed by the formation of the shell was estimated from the thickness of the silica shell assuming a density of 1.2 g.cm^{-3} (similar to the density of ordered mesoporous materials such as MCM-41)~~ number of silica shells equal to the number of AuNRs in the sample, as no uncoated AuNR were observed. TEOS consumption was estimated to 25 % on day 17 (thickness of the silica shell: 14 nm). This calculation is very rough but it still clearly indicates that a large fraction of initially introduced TEOS does neither participate to the formation of the silica shell, nor results in the homogeneous nucleation of core-free silica particles.

The growth of a silica shell at pH=4 is therefore possible but slow due to the very slow TEOS condensation at this pH. It leads, not only to core-shell particles with thick and homogeneous silica shell that exhibits an unconventional porosity, but also prevents homogeneous SiO_2 nucleation.

Silica growth on gold nanorods following Protocol B, *AuNR@⊥m-SiO_2*: In Protocol B, the coating is done without primer and with pH-swing (from 4 to 8), the resulting core-shell NPs exhibit a mesoporosity perpendicular to the gold core and are labelled AuNR@⊥m-SiO_2 (Figure 2). The AuNRs used for this study have average dimensions of 108 × 48 nm (AR = 2.3). As mentioned above, at pH 4, hydrolysis of TEOS is fast, while the condensation reaction is very slow at pH 4 and fast at pH 8 (Figure S 5). Hence, with this protocol these two reactions will occur separately: TEOS will be fully hydrolyzed first (pH=4) with negligible condensation. Then, the condensation of pre-hydrolyzed TEOS will occur rapidly upon increasing the pH to 8. This pH modulation was first done by quickly adding NaOH using a micropipette after TEOS hydrolysis. For this first series of experiments the CTAB concentration was set at 1.1 mM and the results are shown in Figure S 8. At low TEOS concentration (*i.e.* Au/TEOS mole ratio = 1/0.9), the obtained AuNR@⊥m-SiO_2 have a poorly structured silica shell (Figure S 8-a), while higher TEOS concentrations (corresponding to 1/1.8 and 1/3.6 Au/TEOS mole ratios) result in the formation of a uniform silica shell around the AuNRs along with homogeneous nucleation of core-free SiO_2 (Figure S 8-b and c). Silica shell formation led to very small shift of l-LSPR band (Figure S 8-d) and to no visual color change of the solution (inserts in Figure S 8-a, b, and c). Noteworthily, the purification procedure did not allow to remove the core-free SiO_2 particles from the final mixture (Figure S 8-b and c).

Alternatively, in view of improving the protocol, the CTAB concentration was increased to 1.6 mM and pH modulation was automated using a syringe pump for NaOH addition. The AuNRs used for this study have average dimensions of 117 × 43 nm (AR = 2.7). The resulting AuNR@⊥m-SiO_2 synthesized at low TEOS concentration (corresponding to Au/TEOS mole ratio = 1/0.9, Figure 2-a) show a poorly structured silica shell as previously observed, while higher TEOS concentrations (corresponding to 1/1.8 and 1/3.6 Au/TEOS mole ratios) provide

a thick and uniform silica shell of 18.4 ± 3.1 and 22.5 ± 3.3 nm, respectively (Figure 2-b,c, and e for SEM; see Figure S 9, for a high resolution large size micrograph) with a porosity oriented perpendicularly to the AuNR surface. Moreover, using these experimental conditions, core-free silica particles are absent from the purified samples for all Au/TEOS ratios (Figure 2-a, b, c compared to Figure S 8-a, b, c).

The extinction spectra of the AuNR@⊥m-SiO_2 before and after the purification procedure are shown in Figure 2-d. On the spectra recorded before purification, the l-LSPR band position is red-shifted when TEOS amount increases, as observed for protocol A. In addition, and again as seen for protocol A, purification induces a blue-shift of the l-LSPR band position that stabilizes at 751 nm, independently from silica shell thickness. This blue shift is here again attributed to CTAB removal, further evidenced by the negative zeta potential, -27 mV vs. +40 mV before washing (Figure S 9-c), and by Raman and XPS analyses that show a decrease of CTAB bands, and absence of N1s photopeak, respectively (Figure S 3 and S 7-b).

Figure 2: Results for protocol B, TEM images of AuNR@⊥m-SiO_2 synthesized with controlled NaOH addition and [CTAB] = 1.6 mM using different Au/ TEOS ratios. (a) 1/0.9, (b) 1/1.8 and (c) 1/3.6. Scale bar in the insert correspond to 100 nm. (d) Extinction spectra of the original AuNRs and AuNR@⊥m-SiO_2 using different Au/ TEOS ratios before and after washing. (e) SEM image for (c).

As for protocol A, prior to the estimation of the amount of TEOS involved in the shell growth, TEM images of core-shell AuNR@⊥m-SiO_2 were recorded before purification. The images shown in Figure S 9 reveal the occurrence of core-free silica particles for Au/TEOS values of 1/1.8 and 1/3.6 (Figure S 9-e and f), but not for Au/TEOS=1/0.9 (Figure S 9-d), as expected from the fact that homogeneous nucleation of silica requires monomers concentration to be higher than a critical value. Moreover, the fraction of these particles visibly increases upon increasing TEOS concentration. As these core-free silica particles are not observed after purification (Figure 2-b and c and Figure S 9-h and i), one can conclude that they have been removed by centrifugation, thanks to their colloidal stability, their small size and their low density. Their complete elimination is ensured by setting the CTAB concentration high enough (i.e. 1.6 mM) to prevent their agglomeration (Figure S 8-b and c).

The amounts of TEOS solely consumed by shell formation and calculated on the basis of the above described hypotheses were ca. 40 % and 28 % for 1/1.8 and 3.6 Au/TEOS mole ratios, respectively, that is slightly higher than the one calculated for protocol A, despite the consumption of TEOS in core-free silica nanoparticles.

Silica growth on gold nanorods following Protocol C, *AuNR@t-SiO_2*: Several groups have reported the use of MPTMS (Mercaptopropyltrimethoxysilane) as a surface modifier to displace adsorbed CTAB thanks to the formation of strong Au-S bonds at the gold rod surface, while exposing reactive SiOMe and/or SiOH groups at the AuNR surface. In previously reported protocols, this primer was added prior to hydrolysis and condensation of sodium silicate and this type of protocol usually aimed at producing a thin silica shell.[41,42] We have applied the previously described pH-swing method to MPTMS-capped AuNRs. The concentration of CTAB was set at 1.6 mM and AuNRs used for this study have approximate dimensions of 113 × 42 nm (AR = 2.7). MPTMS was first added to the AuNRs suspension at pH 4. Under these conditions, MPTMS displaces CTAB from the gold surface, while the three methoxy groups may undergo hydrolysis to form silanols. This hydrolysis occurs without significant modification of the pH of the suspension. TEOS was then added to the solution allowing its fast hydrolysis. The pH was then increased up to 8 by addition of NaOH with a syringe pump, allowing the condensation reactions to occur.

Figure 3-a, b, and c show representative TEM images of AuNR@t-SiO_2 obtained with increasing TEOS concentrations (1/0.9, 1/1.8 and 1/3.6 Au/TEOS mole ratios, respectively), a SEM micrograph for the highest TEOS amount is also shown (Figure 3-f). Using this protocol, well defined silica shells of increasing thickness (2.1 (± 0.4), 3.4 (± 0.5) and 5.7 (± 0.9) nm) were obtained.

Figure 3: TEM images of AuNR@t-SiO_2 synthesized using MPTMS primer and pH monitoring with different Au/ TEOS ratios and measurement of silica shell thickness. (a) 1/0.9, (b) 1/1.8 and (c) 1/3.6. Scale bar in the insert corresponds to 100 nm. Extinction spectra and first derivative in the insert of the obtained AuNR@t-SiO_2 (d) Before purification and (e) After purification. (f) SEM image for (c).

The optical properties of these AuNR@t-SiO_2 were investigated by UV-Vis spectroscopy, before and after purification (Figure 3-d and e), maximum of the l-LSPR band is indicated in the legend next to the corresponding sample. Before the washing cycle (Figure 3-d), a blue shift of the l-LSPR band upon MPTMS addition suggests ligand exchange with replacement of the CTAB double layer by a MPTMS layer at the particle surface. Adding increasing amounts of TEOS led to a gradual red shift of the l-LSPR band with increasing thickness of the silica shell, as previously observed for protocols A and B. Here again, purification resulted in a blue shift of l-LSPR band, assigned to CTAB removal, for all AuNR@t-SiO_2 samples (Figure 3-e). Zeta potential measurements of AuNR@t-SiO_2 dispersions before and after washing (Figure S 10-a and b) confirmed the silica coating of the nanorods, as the charge surface of AuNRs@SiO_2 changed from positive (+ 44 mV) to negative (- 30 mV) after three washing cycles in EtOH and two cycles in water. Such zeta potential at pH 6.5 matches with the zeta potential of silica particles under the same conditions and thus supports the complete removal of CTAB.[51] CTAB removal for this protocol was also confirmed by SERS and XPS (Figures S 3 and S 7-c).

TEM images of the reaction mixtures before purification of the AuNR@t-SiO_2 are shown on Figure S 10-c, d, and e. For the lowest Au/TEOS ratio, no core-free silica particles were formed (Figure S 10-c). In contrast, the solutions with 1/1.8 and 1/3.6 Au/TEOS mole ratios clearly show the presence of homogeneous silica particles (Figure S 10-d and e). For all Au/TEOS ratios, these particles were removed during purification (Figure S 10-f, g and h). When Protocol C was carried out with 1.1 mM CTAB, TEM images, shown in Figure S 11-a clearly show the presence of silica nanoparticles after purification, while with 1.6 mM CTAB, no free silica are present after purification while the supernatant is solely composed of silica particles (Figure S 11-b and c, respectively). Therefore, as observed for protocol B, 1.6 mM CTAB allows for the total removal of silica nanoparticles.

The silica shell thickness being too thin to allow the appreciation of its porosity by TEM, silica densities of 2.2 $g.cm^{-3}$ (corresponding to dense silica) and 1.2 $g.cm^{-3}$ (corresponding to MCM-41-type porous silica) were used to evaluate the amount of TEOS consumed upon formation of the shell. The yield was ca. 5.0 % (Au/TEOS=0.9), 4.5 % (Au/TEOS=1.8) and 4.0 % (Au/TEOS=3.6) for a porous shell of increasing thickness and to 10.0 %, 8.0 % and 7.0 % for a non-porous shell.

The robustness of the coating protocol was eventually demonstrated by synthesizing AuNR@t-SiO_2 of approx. 3 nm shell thickness from CTAB-capped AuNRs having different sizes using 1/1.8 Au/TEOS mole ratio (Figure 4). The TEM pictures of core-shell AuNR@t-SiO_2 with 3.2 (± 0.5), 3.3 (± 0.6) and 3.6 (± 0.6) nm uniform shell thickness synthesized from AuNRs with approximate dimensions of respectively 109 × 49, 94 × 39 and 102 × 36 nm, show the reproducibility of the protocol regardless of particle size.

Figure 4: TEM images of AuNR@t-SiO_2 synthesized using MPTMS primer and pH monitoring at 1/1.8 Au/TEOS ratio with different AuNR dimensions: (a) 109×49 nm, (b) 94×39 nm and (c) 102×36 nm

Discussion on the three protocols: The AuNR@SiO_2 engineered herein have silica shells of controlled thicknesses and pore organization. We summarized in Table 1 the main features of the silica shells resulting from the three protocols. The pH of the working medium determines the hydrolysis and condensation rates of TEOS. Consequently, it significantly affects the final structure of the shell. It not only determines the kinetics of silica growth (on the AuNR surface and as core-free silica particles by homogeneous nucleation in solution) but also the final pore morphology of the shell. As long as the pH is maintained around 4.0, as for protocol A, the hydrolysis rate is high, and the hydrolyzed species can undergo slow condensation. During the early stages of the reaction (less than five days), due to the slow condensation kinetics, neither silica particles nor silica shell are detected around the AuNRs. After 5 days, an inhomogeneous silica shell becomes clearly visible indicating the onset of silica formation and, after extended reaction time (13 days or more), a mesoporous and thick silica shell is formed. Moreover, for this protocol, no core-free silica particles are detected on the TEM images prior or after purification despite the relatively small fraction of TEOS consumed for silica shell generation (ca. ¼). The absence of homogeneous nucleation of silica particles (despite the high TEOS concentration), suggests that, under conditions that lead to a very slow kinetics of condensation, the homogeneous nucleation of silica is sufficiently delayed to be suppressed in the time frame of our experiments. Surprisingly enough, the silica coating formed at pH=4 develops an unexpected porosity, with pores aligned parallel to the nanorods surface. This is, to the best of our knowledge, the first report of this type of porosity on AuNR@SiO_2. As this coating follows the initial orientation of the CTAB bilayer on the AuNR surface, one can postulate that, under acidic conditions, the original CTAB bilayer controls the growth of the CTAB/silicate mesostructure. The reason why this initial orientation is preserved still needs to be investigated. One can however exclude that it originates from the difference in speciation of silicate species in acidic and basic conditions. Indeed, at pH 4, a pH close to the point of zero charge of silica, the density of charge of silicate species is much lower than at pH 8. But, a low density of charge is, on the contrary, expected to favor a high curvature at the silica/surfactant surface and to favor the formation of a hexagonal over a lamellar phase. Therefore, one can propose that this uncommon orientation of the mesostructure is either related to the slow kinetics of condensation or to a low mobility of CTAB under these experimental conditions.

Table 1: Summary of the main characteristics of the AuNR@SiO_2 particles depending on the experimental conditions

Synthesis protocol	Au/TEOS ratio	[CTAB] (mM)	Reaction time	Shell Thickness (nm)	Porosity	Nucleation of SiO_2 NP	Presence of SiO_2 NP after washing
A //m-SiO_2	1/3.6	1.1	17 days	14	// to the Surface	No	no
B ⊥m-SiO_2	1/0.9	1.1	18h	__*	⊥ to the Surface	no	no
	1/1.8	1.1		13		yes	yes
	1/3.6	1.1		19		yes	yes
	1/0.9	1.6	18h	__*	⊥ to the Surface	no**	no
	1/1.8	1.6		17		yes	no
	1/3.6	1.6		21		yes	no

	1/0.9	1.6		2.1		no**	no
C t-SiO_2	1/1.8	1.6	18h	3.4	Non porous	yes	no
	1/3.6	1.6		5.7		yes	no

* Non Homogeneous layer

** [TEOS] is, in these conditions, likely to be below the critical value for homogeneous nucleation

When the condensation reaction is performed under mildly basic conditions (pH 8), after an initial hydrolysis step at pH 4, as in Protocol B, silica growth is much faster and the silica coating is formed overnight. The pH-swing method was initially proposed by Brinker et al. for the formation of silica gels[52–54] and, more recently investigated in detail by Fidalgo et al.[55–57] to produce highly porous silica xerogels. The pH conditions of this pH-swing protocol differ significantly from those traditionally used in AuNR coating processes derived from the initial work of Gorelikov et al. (which are also similar to those used in the classical Stöber process). Indeed, for all these protocols it is necessary to set the pH for which both hydrolysis and condensation reactions are fast, and these conditions can only be obtained at relatively high pH (pH=10-11) because hydrolysis is very slow at moderately basic pH (pH=7-9) and, according to Abadeer et al., the growth of a silica shell at moderate pH (pH≤9) is not possible.[34] Using the pH-swing method, as TEOS is hydrolyzed first at acidic pH, the condensation reaction can be performed in milder conditions (pH 8) and governs the kinetics of formation of the silica shell. Moreover, as explained by Fidalgo et al., this two-step process favors the formation of highly cross-linked silica (with few residual silanol groups) because both acid-catalyzed hydrolysis and basic-catalyzed condensation favor cross-linking.[56] These changes in the sol-gel chemistry of TEOS may be at the origin of the different morphologies of the pores of the silica shell in our work compared to previously published results (aligned pores with an orientation perpendicular to the AuNR surface for protocol A compared to a more disordered pore morphology in previous works), but the precise origin of this higher pore organization remains unclear.

In the present work we have associated this pH-swing protocol to two different concentrations of CTAB: 1.1 mM (corresponding to the concentration used by Wu et al. in their work[36]) and 1.6 mM. For samples prepared from the same TEOS concentration, the thickness of the silica coating is in the same range: 13/19 and 17/21 nm for 1.1 and 1.6, respectively (Table 1) and these samples differ only for the presence of core-free silica particles in the purified samples for Au/TEOS ratios of 1/1.8 and 1/3.6. A high CTAB concentration seems therefore mandatory for the successful removal of core-free silica particles, possibly due to a better colloidal stability of these particles when surrounded by CTAB.

The last series of AuNR@SiO_2 associates MPTMS as primer with the pH-swing method, protocol C. A thin and extremely homogeneous silica coating was obtained for all Au/TEOS ratios with a regular increase of the thickness of the silica coating with increasing the amount of TEOS. For the samples synthesized with [CTAB] = 1.6 mM, the core-free silica particles observed on TEM images of the raw samples for Au/TEOS = 1.8 and 3.6, are fully removed in the purified samples.

On the basis of calculations and the absence of core-free silica particles by TEM, Wu and Tracy have concluded that all of the TEOS molecules were consumed to form the silica shells.[36] However, their calculation assumes a silica density of 1.7 $g.cm^{-3}$ which, without being impossible, is higher than that expected for a mesoporous material similar to MCM-41 (pore volume between 0.5 and 1 $cm^3.g^{-1}$, which corresponds to much lower apparent densities

(between 0.8 and 1.2)). If a density of 1 instead of 1.7 is considered, a non-negligible amount of silica is not integrated into the silica shells surrounding gold particles and could be in the form of silica nanoparticles that would have been removed during washing.

For most of the experimental conditions reported herein, we observed silica particles formed by homogeneous nucleation. Interestingly, according to the classical model of nucleation and growth, these ultra-small and monodisperse silica nanoparticles are likely formed during a single burst of nucleation with limited further growth due to rapid consumption of all silica precursors.[58] Hence, during these syntheses, silica particles and the silica coating may form simultaneously. This may appear as a drawback compared to the classical protocols. However, formation of undesired core-free silica particles has already been observed for many of the protocols derived from the initial work of Gorelikov.[33,34,38,59,60] Moreover, these particles, which were observed on the TEM images of the purified samples, may represent only a small fraction of the initially formed core-free silica particles because, as already stated by Abadeer et al., most of them are, thanks to their lower weight, removed from the samples by differential centrifugation.[34] Several protocols successfully produced AuNR@SiO_2 samples devoid of silica particles, usually by a careful control of the amount of added TEOS (the formation of these particles is favored at high TEOS concentration) and the speed of addition of the TEOS solution (stepwise[33,38,42,60] or slow[36] addition of TEOS is often used as a means to keep the silica concentration in solution below the homogeneous nucleation threshold). However, while these protocols require a very careful control of the experimental conditions, our work suggests that, rather than preventing the homogeneous nucleation of silica, an easier approach could be to choose synthesis conditions allowing their total elimination upon purification. In this approach, CTAB concentration plays a key role: with a CTAB concentration of 1.1 mM, the purified samples still contain core-free silica particles while they do not when [CTAB]=1.6 mM. This CTAB concentration is higher than the values suggested in many protocols (usually below 1.2 mM).[33,34,36] CTAB not only acts as a soft template (leading to the formation of the porous silica coating) but also as a stabilizer of the colloidal particles (AuNR@SiO_2 and core-free SiO_2 particles) present in the solution. With an appropriate amount of CTAB, the positive charge of CTAB molecules present at the surface of core-free and core-shell silica particles leads to a strong electrostatic repulsion between all colloidal particles and prevents aggregation. The lighter core-free silica particles can then be readily removed by differential centrifugation. In what follows we explore the potentialities of AuNR@ t-SiO_2 in LSPR immunosensing.

Toward the development of AuNR@ t-SiO_2-based immunosensor: The underlying principle of gold nanoparticle-based LSPR biosensors relies on the sensitivity of the plasmon band position to the refractive index of the surrounding medium and the distance dependence of the band shift. These properties enable separation-free bioassays since only binding events that occur at close proximity of the nanoparticles will contribute to the plasmon band shift.[9] Surprisingly, very few examples of AuNR@SiO_2-based LSPR immunosensors have been reported to date.[61,62]

As a preliminary experiment to the setup of a solution-phase LSPR biosensor based on AuNR@ t-SiO_2, its refractive index sensitivity was determined by measuring the shift of the LSPR band position in aqueous solutions containing an increasing proportion of glycerol (Figure 5 a-c). A sensitivity value of 326 nm/RIU (Refractive Index Unit) was calculated, in excellent agreement with values reported in the literature for thin shells of SiO_2 on AuNR[62]. Of note, this sensitivity value is also larger by ca ~ 30% than that of the starting AuNR which is 274 nm/RIU which suggests a higher efficiency for the silica coated materials in biosensing.

Figure 5: Normalized extinction spectra of (a) CTAB-capped AuNR and (b) AuNR@t-SiO_2 in water-glycerol mixtures of varying fractions; (c) Dependence of the longitudinal plasmon shift of CTAB-capped AuNR (black squares) and AuNR@t-SiO_2 (red squares) on refractive index of liquid mixtures. (d) and (e) Normalized extinction spectra of the nanoimmunoprobes before and after target recognition and their derivatives.

A nanoimmunoprobe was next constructed by physisorption of goat anti-rabbit IgG antibody (Ab) to AuNR@ t-SiO_2 with the objective of setting up a solution-phase, homogenous and label-free immunoassay of the model antigen rabbit IgG (Target) as described in Figure S12 a. The binding of the target to the nanoimmunoprobe should result in a change of the refractive index at the vicinity of the nanoparticles and in turn to a shift of the LSPR band position measurable by a UV-visible spectrometer. The construction of the nanoimmunoprobe was performed through successive additions of Ab and BSA to a colloidal solution of AuNR@ t-SiO_2. These additions resulted in a shift of the LSPR band position from 716 to ca. 730 nm (see Figure S12 b). This red shift is related to the higher refractive index of proteins as compared to water. Simultaneously, the zeta potential increased from -32.0 ± 1.9 to -15.0 ± 0.7 mV. The average number of Ab bound to AuNR@ t-SiO_2 was 135 ± 48 as indirectly assayed by spectrofluorimetry with a fluorescein-labeled Ab following a previously reported method[63].

Finally, the target, a Rabbit IgG, was added to a suspension of the nanoimmunoprobe in phosphate buffer pH 7.4 at a concentration of 500 ng/mL. Figure 5 d and e show the extinction spectra measured before and after target addition and their first derivatives. A clear shift of the LSPR band position to the red was observed corresponding to a $\Delta\lambda_{LSPR}$ of 5 nm. This band shift was unambiguously assigned to the successful binding of the target to the nanoimmunoprobe inducing a change of the refractive index since so such shift was noticed when the nanoimmunoprobe was incubated with a non-specific target (data not shown). These results clearly show that the AuNR@t-SiO_2 nanoparticles can be applied for antibodies immobilization and that the silica shell is thin enough to preserve the plasmonic sensitivity and allow LSPR readout of target recognition.

CONCLUSIONS

In summary, we have reported a versatile method for the synthesis of core-shell AuNR@SiO_2 nanoparticles with tailored shell thickness and porosity. By modulating the pH of the reaction medium, control over the silica growth rate and morphological parameters of the shell was achieved. Different silica shell thicknesses, from 13 to 21 nm, were produced by varying the Au/TEOS ratio. Depending on the pH set for TEOS condensation, the orientation of the silica porosity was tailored to be either perpendicular, or, more unexpectedly, parallel to AuNRs surface. Finally, the use of a surface primer allowed the formation of ultrathin non porous silica shells with a thickness precisely tunable between 2 and 6 nm by varying Au/TEOS ratio. In all the synthesis methods optimized here, the colloidal stability and optical properties of the plasmonic core were preserved. In addition, we show that the formation of SiO_2 nanoparticles cannot be avoided in alkaline medium when homogeneous nucleation threshold is reached. CTAB concentration was shown to play a major role to efficiently remove SiO_2 nanoparticles during the purification steps. By combining XPS, Raman and zeta potential measurements, we evidenced the total removal of CTAB during washing steps, which will facilitate the potential use of these AuNR@SiO_2 in biological media. The formation of ultrathin silica shell showed a promising potential for the development of LSPR biosensors. Indeed, their RI sensitivity factor was 30 % higher than that of bare AuNRs. In addition, preliminary immunosensing experiments

allowed the successful adsorption of antibodies and the further recognition of a model target and clearly showed the silica shell was thin enough to preserve the plasmonic sensitivity of the nanoimmunoprobes. Furthermore, we expect the original onion-shaped porosity parallel to AuNRs surface developed here to provide interesting vehicles for drug delivery and further release of embedded molecules and intend to explore these potentialities in our upcoming studies.

SUPPORTING INFORMATION

ACKNOWLEDGMENT

This work was financially supported by the National Research Agency (project n° ANR- 16-CE07-0031-01). Y. Mazouzi and S. Casale are thanked for their help in TEM and SEM measurements.

ABBREVIATIONS

APTMS : 3-aminopropyltrimethoxysilane
AR: Aspect ratio
AuNRs: Gold nanorods
AuNR@SiO_2: Silica-coated gold nanorod
AuNR@//m-SiO_2: Gold nanorod coated with a mesoporous silica shell having pores oriented parallelly to the gold surface
AuNR@⊥m-SiO_2: Gold nanorod coated with a mesoporous silica shell having pores oriented perpendicularly to the gold surface
AuNR@t-SiO_2: Gold nanorod coated with a thin silica shell
BSA: bovine serum albumin
CTAB: Cetyltrimethylammonium bromide
DLS: Dynamic light scattering
ELS: Electrophoretic Light Scattering
IgG: immunoglobulin G
LSPR: Localized surface plasmon resonance
l-LSPR: Longitudinal localized surface plasmon resonance
mPEG-SH: O-[2-(3-Mercaptopropionylamino)ethyl]-O′-methylpolyethylene glycol
MPTMS: 3-Mercaptopropyltrimethoxysilane
NaOL: Sodium oleate
RI: Refractive Index
RIU: Refractive Index Unit
SEM: Scanning electron microscopy
SERS: Surface enhanced Raman scattering
TEM: Transmission electronic microscopy
TEOS: Tetraethylorthosilicate
t-LSPR: Transverse localized surface plasmon resonance
UV-Vis: UV-Visible
XPS: X-ray photoelectron spectroscopy

REFERENCES

(1) Pérez-Juste, J.; Pastoriza-Santos, I.; Liz-Marzán, L.; Mulvaney, P. Gold Nanorods: Synthesis, Characterization and Applications. *Coord. Chem. Rev.* **2005**, *249* (17–18), 1870–1901. https://doi.org/10.1016/j.ccr.2005.01.030.

(2) Huang, X.; Neretina, S.; El-Sayed, M. A. Gold Nanorods: From Synthesis and Properties to Biological and Biomedical Applications. *Adv. Mater.* **2009**, *21* (48), 4880–4910. https://doi.org/10.1002/adma.200802789.

(3) Link, S.; Mohamed, M. B.; El-Sayed, M. A. Simulation of the Optical Absorption Spectra of Gold Nanorods as a Function of Their Aspect Ratio and the Effect of the Medium Dielectric Constant. *J. Phys. Chem. B* **1999**, *103* (16), 3073–3077. https://doi.org/10.1021/jp990183f.

(4) Chang, H.-H.; Murphy, C. J. Mini Gold Nanorods with Tunable Plasmonic Peaks beyond 1000 Nm. *Chem. Mater.* **2018**, *30* (4), 1427–1435. https://doi.org/10.1021/acs.chemmater.7b05310.

(5) Weissleder, R. A Clearer Vision for in Vivo Imaging. *Nat. Biotechnol.* **2001**, *19* (4), 316–317. https://doi.org/10.1038/86684.

(6) Chen, H.; Kou, X.; Yang, Z.; Ni, W.; Wang, J. Shape- and Size-Dependent Refractive Index Sensitivity of Gold Nanoparticles. *Langmuir* **2008**, *24* (10), 5233–5237. https://doi.org/10.1021/la800305j.

(7) Burrows, N. D.; Harvey, S.; Idesis, F. A.; Murphy, C. J. Understanding the Seed-Mediated Growth of Gold Nanorods through a Fractional Factorial Design of Experiments. *Langmuir* **2017**, *33* (8), 1891–1907. https://doi.org/10.1021/acs.langmuir.6b03606.

(8) Leng, Y.; Yin, X.; Hu, F.; Zou, Y.; Xing, X.; Li, B.; Guo, Y.; Ye, L.; Lu, Z. High-Yield Synthesis and Fine-Tuning Aspect Ratio of (200) Faceted Gold Nanorods by the PH-Adjusting Method. *RSC Adv.* **2017**, *7* (41), 25469–25474. https://doi.org/10.1039/C7RA04051B.

(9) Pellas, V.; Hu, D.; Mazouzi, Y.; Mimoun, Y.; Blanchard, J.; Guibert, C.; Salmain, M.; Boujday, S. Gold Nanorods for LSPR Biosensing: Synthesis, Coating by Silica, and Bioanalytical Applications. *Biosensors* **2020**, *10* (10), 146. https://doi.org/10.3390/bios10100146.

(10) Lohse, S. E.; Murphy, C. J. The Quest for Shape Control: A History of Gold Nanorod Synthesis. *ACS Chem. Mater.* **2013**, *25* (8), 1250–1261. https://doi.org/10.1021/cm303708p.

(11) Connor, E. E.; Mwamuka, J.; Gole, A.; Murphy, C. J.; Wyatt, M. D. Gold Nanoparticles Are Taken Up by Human Cells but Do Not Cause Acute Cytotoxicity. *Small* **2005**, *1* (3), 325–327. https://doi.org/10.1002/smll.200400093.

(12) Mirska, D.; Schirmer, K.; Funari, S. S.; Langner, A.; Dobner, B.; Brezesinski, G. Biophysical and Biochemical Properties of a Binary Lipid Mixture for DNA

Transfection. *Colloids Surf. B Biointerfaces* **2005**, *40* (1), 51–59. https://doi.org/10.1016/j.colsurfb.2004.10.007.

(13) Alkilany, A. M.; Nagaria, P. K.; Hexel, C. R.; Shaw, T. J.; Murphy, C. J.; Wyatt, M. D. Cellular Uptake and Cytotoxicity of Gold Nanorods: Molecular Origin of Cytotoxicity and Surface Effects. *Small* **2009**, *5* (6), 701–708. https://doi.org/10.1002/smll.200801546.

(14) Jia, Y. P.; Shi, K.; Liao, J. F.; Peng, J. R.; Hao, Y.; Qu, Y.; Chen, L. J.; Liu, L.; Yuan, X.; Qian, Z. Y.; Wei, X. W. Effects of Cetyltrimethylammonium Bromide on the Toxicity of Gold Nanorods Both In Vitro and In Vivo: Molecular Origin of Cytotoxicity and Inflammation. *Small Methods* **2020**, *4* (3), 1900799. https://doi.org/10.1002/smtd.201900799.

(15) Fernández-Lodeiro, A.; Djafari, J.; Fernández-Lodeiro, J.; Duarte, M. P.; Muchagato Mauricio, E.; Capelo-Martínez, J. L.; Lodeiro, C. Synthesis of Mesoporous Silica Coated Gold Nanorods Loaded with Methylene Blue and Its Potentials in Antibacterial Applications. *Nanomaterials* **2021**, *11* (5), 1338. https://doi.org/10.3390/nano11051338.

(16) Han, H.-W.; Joe, A.; Jang, E.-S. Reduced Cytotoxicity of CTAB-Templated Silica Layer on Gold Nanorod Using Fluorescence Dyes and Its Application in Cancer Theranostics. *J. Ind. Eng. Chem.* **2021**, *96*, 202–212. https://doi.org/10.1016/j.jiec.2021.01.020.

(17) Albrecht, W.; van de Glind, A.; Yoshida, H.; Isozaki, Y.; Imhof, A.; van Blaaderen, A.; de Jongh, P. E.; de Jong, K. P.; Zečević, J.; Takeda, S. Impact of the Electron Beam on the Thermal Stability of Gold Nanorods Studied by Environmental Transmission Electron Microscopy. *Ultramicroscopy* **2018**, *193*, 97–103. https://doi.org/10.1016/j.ultramic.2018.05.006.

(18) Boujday, S.; Lambert, J.-F.; Che, M. Amorphous Silica as a Versatile Supermolecular Ligand for NiII Amine Complexes: Toward Interfacial Molecular Recognition. *ChemPhysChem* **2004**, *5* (7), 1003–1013. https://doi.org/10.1002/cphc.200400008.

(19) Wang, Z.; Zong, S.; Yang, J.; Li, J.; Cui, Y. Dual-Mode Probe Based on Mesoporous Silica Coated Gold Nanorods for Targeting Cancer Cells. *Biosens. Bioelectron.* **2011**, *26* (6), 2883–2889. https://doi.org/10.1016/j.bios.2010.11.032.

(20) Mallick, S.; Sun, I.-C.; Kim, K.; Yi, D. K. Silica Coated Gold Nanorods for Imaging and Photo-Thermal Therapy of Cancer Cells. *J. Nanosci. Nanotechnol.* **2013**, *13* (5), 3223–3229. https://doi.org/10.1166/jnn.2013.7149.

(21) Chen, Y.-S.; Frey, W.; Kim, S.; Homan, K.; Kruizinga, P.; Sokolov, K.; Emelianov, S. Enhanced Thermal Stability of Silica-Coated Gold Nanorods for Photoacoustic Imaging and Image-Guided Therapy. *Opt. Express* **2010**, *18* (9), 8867–8878. https://doi.org/10.1364/OE.18.008867.

(22) Gergely-Fülöp, E.; Zámbó, D.; Deák, A. Thermal Stability of Mesoporous Silica-Coated Gold Nanorods with Different Aspect Ratios. *Mater. Chem. Phys.* **2014**, *148* (3), 909–913. https://doi.org/10.1016/j.matchemphys.2014.08.069.

(23) Lim, S.-H.; Lee, M.-J.; Kang, S.-H.; Dey, J.; Umar, A.; Lee, S.-J.; Choi, S.-M. Individually Silica-Embedded Gold Nanorod Superlattice for High Thermal and Solvent Stability and Recyclable SERS Application. *Adv. Mater. Interfaces* **2019**, *6* (21), 1900986. https://doi.org/10.1002/admi.201900986.

(24) Chen, Y.-S.; Frey, W.; Kim, S.; Kruizinga, P.; Homan, K.; Emelianov, S. Silica-Coated Gold Nanorods as Photoacoustic Signal Nanoamplifiers. *Nano Lett.* **2011**, *11* (2), 348–354. https://doi.org/10.1021/nl1042006.

(25) Alkurdi, A.; Lombard, J.; Detcheverry, F.; Merabia, S. Enhanced Heat Transfer with Metal-Dielectric Core-Shell Nanoparticles. *Phys. Rev. Appl.* **2020**, *13* (3), 034036. https://doi.org/10.1103/PhysRevApplied.13.034036.

(26) Guerrero-Martínez, A.; Pérez-Juste, J.; Liz-Marzán, L. M. Recent Progress on Silica Coating of Nanoparticles and Related Nanomaterials. *Adv. Mater.* **2010**, *22* (11), 1182–1195. https://doi.org/10.1002/adma.200901263.

(27) Slowing, I. I.; Trewyn, B. G.; Giri, S.; Lin, V. S.-Y. Mesoporous Silica Nanoparticles for Drug Delivery and Biosensing Applications. *Adv. Funct. Mater.* **2007**, *17* (8), 1225–1236. https://doi.org/10.1002/adfm.200601191.

(28) Zhang, Z.; Wang, L.; Wang, J.; Jiang, X.; Li, X.; Hu, Z.; Ji, Y.; Wu, X.; Chen, C. Mesoporous Silica-Coated Gold Nanorods as a Light-Mediated Multifunctional Theranostic Platform for Cancer Treatment. *Adv. Mater.* **2012**, *24* (11), 1418–1423. https://doi.org/10.1002/adma.201104714.

(29) Ben Haddada, M.; Hu, D.; Salmain, M.; Zhang, L.; Peng, C.; Wang, Y.; Liedberg, B.; Boujday, S. Gold Nanoparticle-Based Localized Surface Plasmon Immunosensor for Staphylococcal Enterotoxin A (SEA) Detection. *Anal. Bioanal. Chem.* **2017**, *409* (26), 6227–6234. https://doi.org/10.1007/s00216-017-0563-8.

(30) Loiseau, A.; Zhang, L.; Hu, D.; Salmain, M.; Mazouzi, Y.; Flack, R.; Liedberg, B.; Boujday, S. Core–Shell Gold/Silver Nanoparticles for Localized Surface Plasmon Resonance-Based Naked-Eye Toxin Biosensing. *ACS Appl. Mater. Interfaces* **2019**, *11* (50), 46462–46471. https://doi.org/10.1021/acsami.9b14980.

(31) Stöber, W.; Fink, A.; Bohn, E. Controlled Growth of Monodisperse Silica Spheres in the Micron Size Range. *J. Colloid Interface Sci.* **1968**, *26* (1), 62–69. https://doi.org/10.1016/0021-9797(68)90272-5.

(32) Gorelikov, I.; Matsuura, N. Single-Step Coating of Mesoporous Silica on Cetyltrimethyl Ammonium Bromide-Capped Nanoparticles. *Nano Lett.* **2008**, *8* (1), 369–373. https://doi.org/10.1021/nl0727415.

(33) DuChene, J. S.; Almeida, R. P.; Wei, W. D. Facile Synthesis of Anisotropic Au@SiO2 Core–Shell Nanostructures. *Dalton Trans.* **2012**, *41* (26), 7879–7882. https://doi.org/10.1039/C2DT30409K.

(34) Abadeer, N. S.; Brennan, M. R.; Wilson, W. L.; Murphy, C. J. Distance and Plasmon Wavelength Dependent Fluorescence of Molecules Bound to Silica-Coated Gold Nanorods. *ACS Nano* **2014**, *8* (8), 8392–8406. https://doi.org/10.1021/nn502887j.

(35) Liu, J.; Kan, C.; Cong, B.; Xu, H.; Ni, Y.; Li, Y.; Shi, D. Plasmonic Property and Stability of Core-Shell Au@SiO2 Nanostructures. *Plasmonics* **2014**, *9* (5), 1007–1014. https://doi.org/10.1007/s11468-014-9708-1.

(36) Wu, W.-C.; Tracy, J. B. Large-Scale Silica Overcoating of Gold Nanorods with Tunable Shell Thicknesses. *ACS Chem. Mater.* **2015**, *27* (8), 2888–2894. https://doi.org/10.1021/cm504764v.

(37) Rowe, L. R.; Chapman, B. S.; Tracy, J. B. Understanding and Controlling the Morphology of Silica Shells on Gold Nanorods. *Chem. Mater.* **2018**, *30* (18), 6249–6258. https://doi.org/10.1021/acs.chemmater.8b00794.

(38) Yoon, S.; Lee, B.; Kim, C.; Lee, J. H. Controlled Heterogeneous Nucleation for Synthesis of Uniform Mesoporous Silica-Coated Gold Nanorods with Tailorable Rotational Diffusion and 1 Nm-Scale Size Tunability. *Cryst. Growth Des.* **2018**, *18* (8), 4731–4736. https://doi.org/10.1021/acs.cgd.8b00724.

(39) Li, J. F.; Tian, X. D.; Li, S. B.; Anema, J. R.; Yang, Z. L.; Ding, Y.; Wu, Y. F.; Zeng, Y. M.; Chen, Q. Z.; Ren, B. Surface Analysis Using Shell-Isolated Nanoparticle-Enhanced Raman Spectroscopy. *Nat. Protoc.* **2013**, *8* (1), 52.

(40) Pérez-Juste, J.; Correa-Duarte, M. A.; Liz-Marzán, L. M. Silica Gels with Tailored, Gold Nanorod-Driven Optical Functionalities. *Appl. Surf. Sci.* **2004**, *226* (1–3), 137–143. https://doi.org/10.1016/j.apsusc.2003.11.013.

(41) Obare, S. O.; Jana, N. R.; Murphy, C. J. Preparation of Polystyrene- and Silica-Coated Gold Nanorods and Their Use as Templates for the Synthesis of Hollow Nanotubes. *Nano Lett.* **2001**, *1* (11), 601–603. https://doi.org/10.1021/nl0156134.

(42) Li, C.; Li, Y.; Ling, Y.; Lai, Y.; Wu, C.; Zhao, Y. Exploration of the Growth Process of Ultrathin Silica Shells on the Surface of Gold Nanorods by the Localized Surface Plasmon Resonance. *Nanotechnology* **2014**, *25* (4), 045704. https://doi.org/10.1088/0957-4484/25/4/045704.

(43) Fernández-López, C.; Mateo-Mateo, C.; Álvarez-Puebla, R. A.; Pérez-Juste, J.; Pastoriza-Santos, I.; Liz-Marzán, L. M. Highly Controlled Silica Coating of PEG-Capped Metal Nanoparticles and Preparation of SERS-Encoded Particles. *Langmuir* **2009**, *25* (24), 13894–13899. https://doi.org/10.1021/la9016454.

(44) Pastoriza-Santos, I.; Pérez-Juste, J.; Liz-Marzán, L. M. Silica-Coating and Hydrophobation of CTAB-Stabilized Gold Nanorods. *ACS Chem. Mater.* **2006**, *18* (10), 2465–2467. https://doi.org/10.1021/cm060293g.

(45) Brinker, C. J. Hydrolysis and Condensation of Silicates: Effects on Structure. *J. Non-Cryst. Solids* **1988**, *100* (1), 31–50. https://doi.org/10.1016/0022-3093(88)90005-1.

(46) Ye, X.; Zheng, C.; Chen, J.; Gao, Y.; Murray, C. B. Using Binary Surfactant Mixtures To Simultaneously Improve the Dimensional Tunability and Monodispersity in the Seeded Growth of Gold Nanorods. *Nano Lett* **2013**, *13* (2), 765–771. https://doi.org/10.1021/nl304478h.

(47) Scarabelli, L.; Grzelczak, M.; Liz-Marzán, L. M. Tuning Gold Nanorod Synthesis through Prereduction with Salicylic Acid. *ACS Chem. Mater.* **2013**, *25* (21), 4232–4238. https://doi.org/10.1021/cm402177b.

(48) Hendel, T.; Wuithschick, M.; Kettemann, F.; Birnbaum, A.; Rademann, K.; Polte, J. In Situ Determination of Colloidal Gold Concentrations with UV–Vis Spectroscopy: Limitations and Perspectives. *ACS Anal. Chem.* **2014**, *86* (22), 11115–11124. https://doi.org/10.1021/ac502053s.

(49) Wang, W.; Wang, P.; Tang, X.; Elzatahry, A. A.; Wang, S.; Al-Dahyan, D.; Zhao, M.; Yao, C.; Hung, C.-T.; Zhu, X.; Zhao, T.; Li, X.; Zhang, F.; Zhao, D. Facile Synthesis of Uniform Virus-like Mesoporous Silica Nanoparticles for Enhanced Cellular Internalization. *ACS Cent. Sci.* **2017**, *3* (8), 839–846. https://doi.org/10.1021/acscentsci.7b00257.

(50) Liz-Marzán, L. M.; Giersig, M.; Mulvaney, P. Synthesis of Nanosized Gold−Silica Core−Shell Particles. *Langmuir* **1996**, *12* (18), 4329–4335. https://doi.org/10.1021/la9601871.

(51) Júnior, J. A. A.; Baldo, J. B. The Behavior of Zeta Potential of Silica Suspensions. *New J. Glass Ceram.* **2014**, *4* (2), 29–37. https://doi.org/10.4236/njgc.2014.42004.

(52) Brinker, C. J.; Keefer, K. D.; Schaefer, D. W.; Ashley, C. S. Sol-Gel Transition in Simple Silicates. *J. Non-Cryst. Solids* **1982**, *48* (1), 47–64. https://doi.org/10.1016/0022-3093(82)90245-9.

(53) Brinker, C. J.; Keefer, K. D.; Schaefer, D. W.; Assink, R. A.; Kay, B. D.; Ashley, C. S. Sol-Gel Transition in Simple Silicates II. *J. Non-Cryst. Solids* **1984**, *63* (1), 45–59. https://doi.org/10.1016/0022-3093(84)90385-5.

(54) Brinker, C. J.; Tallant, D. R.; Roth, E. P.; Ashley, C. S. Sol-Gel Transition in Simple Silicates: III. Structural Studies during Densification. *J. Non-Cryst. Solids* **1986**, *82* (1), 117–126. https://doi.org/10.1016/0022-3093(86)90119-5.

(55) Fidalgo, A.; Ilharco, L. M. Correlation between Physical Properties and Structure of Silica Xerogels. *J. Non-Cryst. Solids* **2004**, *347* (1), 128–137. https://doi.org/10.1016/j.jnoncrysol.2004.07.059.

(56) Fidalgo, A.; Ilharco, L. M. Chemical Tailoring of Porous Silica Xerogels: Local Structure by Vibrational Spectroscopy. *Chem. – Eur. J.* **2004**, *10* (2), 392–398. https://doi.org/10.1002/chem.200305079.

(57) Fidalgo, A.; Rosa, M. E.; Ilharco, L. M. Chemical Control of Highly Porous Silica Xerogels: Physical Properties and Morphology. *ACS Chem. Mater.* **2003**, *15* (11), 2186–2192. https://doi.org/10.1021/cm031013p.

(58) Ding, T.; Yao, L.; Liu, C. Kinetically-Controlled Synthesis of Ultra-Small Silica Nanoparticles and Ultra-Thin Coatings. *Nanoscale* **2016**, *8* (8), 4623–4627. https://doi.org/10.1039/C5NR08224B.

(59) Huang, C.-C.; Huang, C.-H.; Kuo, I.-T.; Chau, L.-K.; Yang, T.-S. Synthesis of Silica-Coated Gold Nanorod as Raman Tags by Modulating Cetyltrimethylammonium Bromide Concentration. *Colloids Surf. Physicochem. Eng. Asp.* **2012**, *409*, 61–68. https://doi.org/10.1016/j.colsurfa.2012.06.003.

(60) Huang, C.-M.; Chung, M.-F.; Souris, J. S.; Lo, L.-W. Controlled Epitaxial Growth of Mesoporous Silica/Gold Nanorod Nanolollipops and Nanodumb-Bells. *APL Mater.* **2014**, *2* (11), 113312. https://doi.org/10.1063/1.4898415.

(61) Wang, C.; Ma, Z.; Wang, T.; Su, Z. Synthesis, Assembly, and Biofunctionalization of Silica-Coated Gold Nanorods for Colorimetric Biosensing. *Adv. Funct. Mater.* **2006**, *16* (13), 1673–1678. https://doi.org/10.1002/adfm.200500898.

(62) Song, L.; Zhang, L.; Huang, Y.; Chen, L.; Zhang, G.; Shen, Z.; Zhang, J.; Xiao, Z.; Chen, T. Amplifying the Signal of Localized Surface Plasmon Resonance Sensing for the Sensitive Detection of Escherichia Coli O157:H7. *Sci. Rep.* **2017**, *7* (1), 3288. https://doi.org/10.1038/s41598-017-03495-1.

(63) Zhang, L.; Hu, D.; Salmain, M.; Liedberg, B.; Boujday, S. Direct Quantification of Surface Coverage of Antibody in IgG-Gold Nanoparticles Conjugates. *Talanta* **2019**, *204*, 875–881. https://doi.org/10.1016/j.talanta.2019.05.104.

Scheme 1

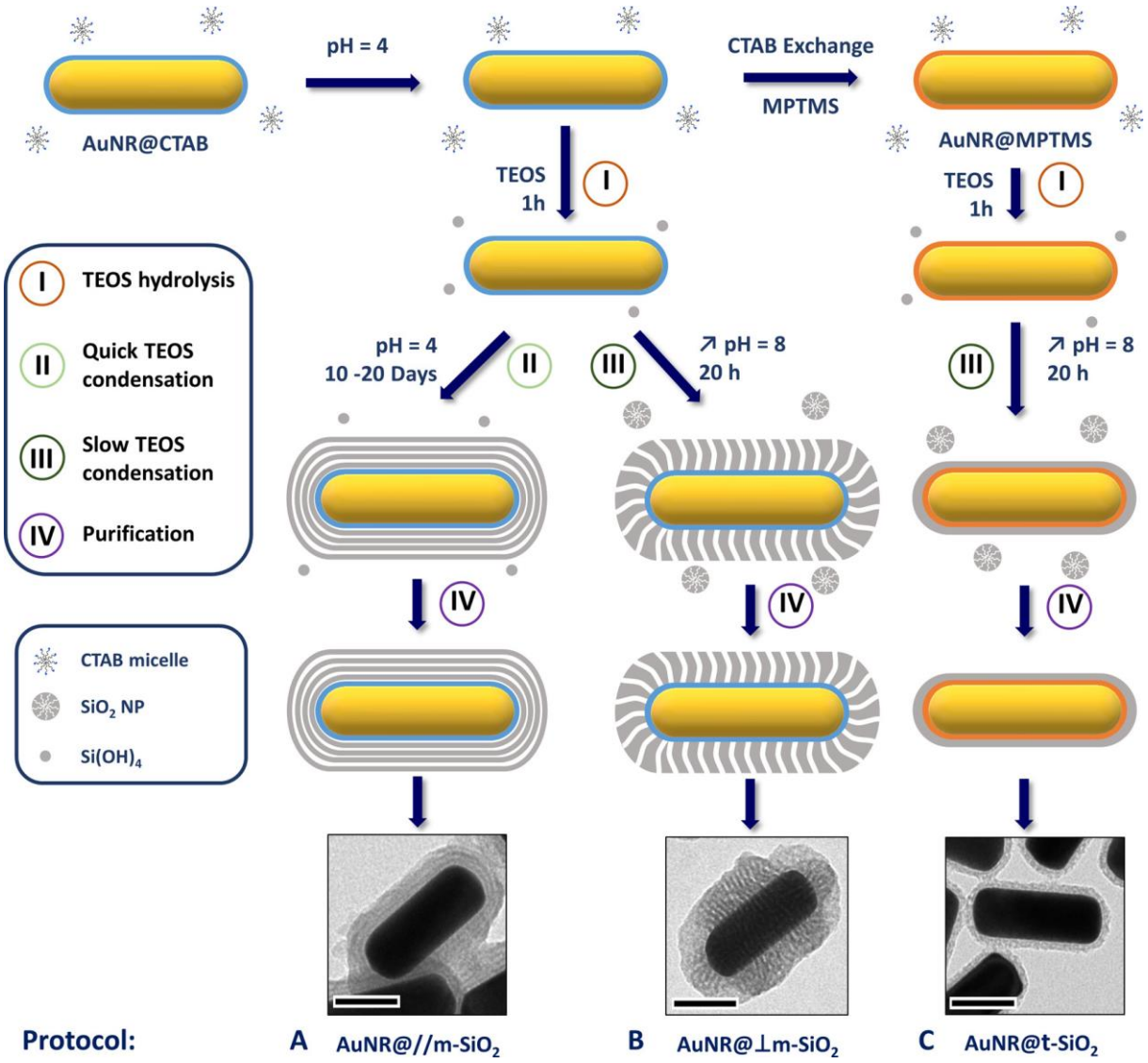

Scheme 1. Pathways Adopted for the Three Protocols Developed to Grow a Silica Shell on AuNRs: (A) AuNR@//m-SiO_2, (B) AuNR@⊥m-SiO_2, and (C) AuNR@t-SiO_2

Figure 1

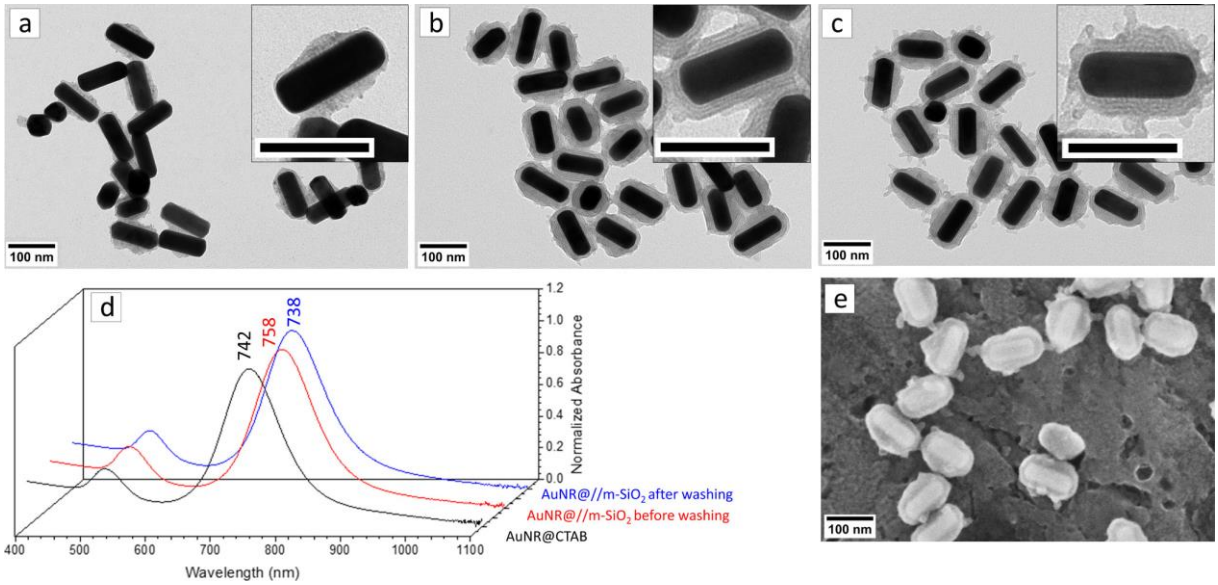

Figure 1. Results for protocol A, AuNR@//m-SiO_2: (a–c) TEM images taken at different reaction times: 5, 13, and 17 days, respectively. Scale bar in the inset corresponds to 100 nm. (d) Extinction spectra of the original AuNRs and AuNR@//m-SiO_2 before and after washing for 17 days reaction time. (e) SEM images for (c).

Figure 2

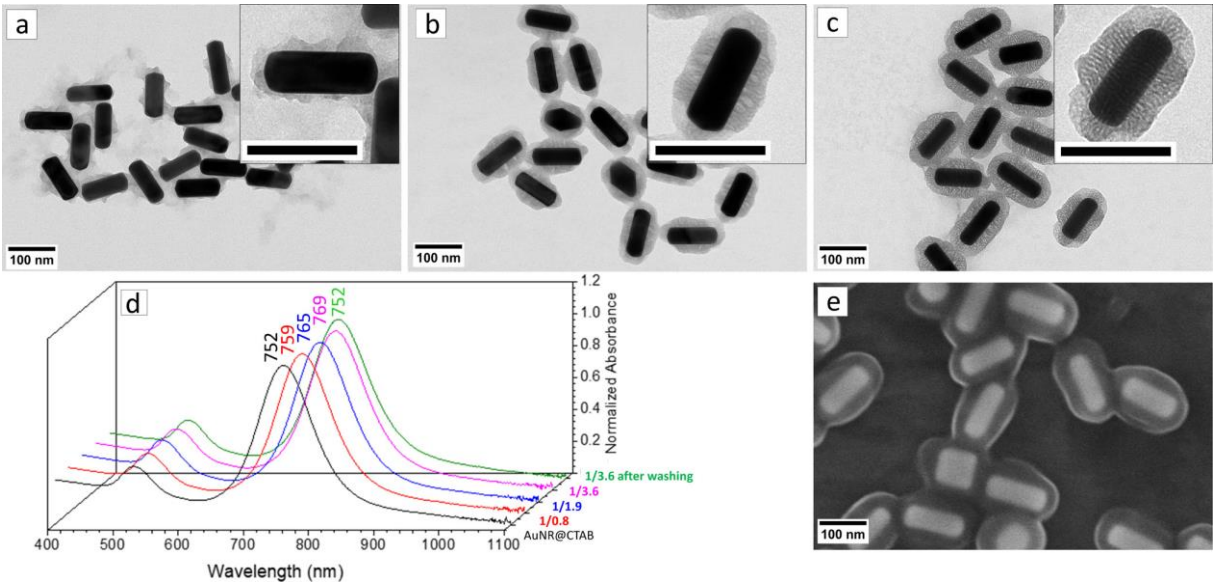

Figure 2. Results for protocol B, TEM images of AuNR@⊥m-SiO_2 synthesized with controlled NaOH addition and [CTAB] of 1.6 mM using different Au/TEOS ratios: (a) 1/0.9, (b) 1/1.8, and (c) 1/3.6. Scale bars in the inset correspond to 100 nm. (d) Extinction spectra of the original AuNRs and AuNR@⊥m-SiO_2 using different Au/TEOS ratios before and after washing. (e) SEM image for (c).

Figure 3

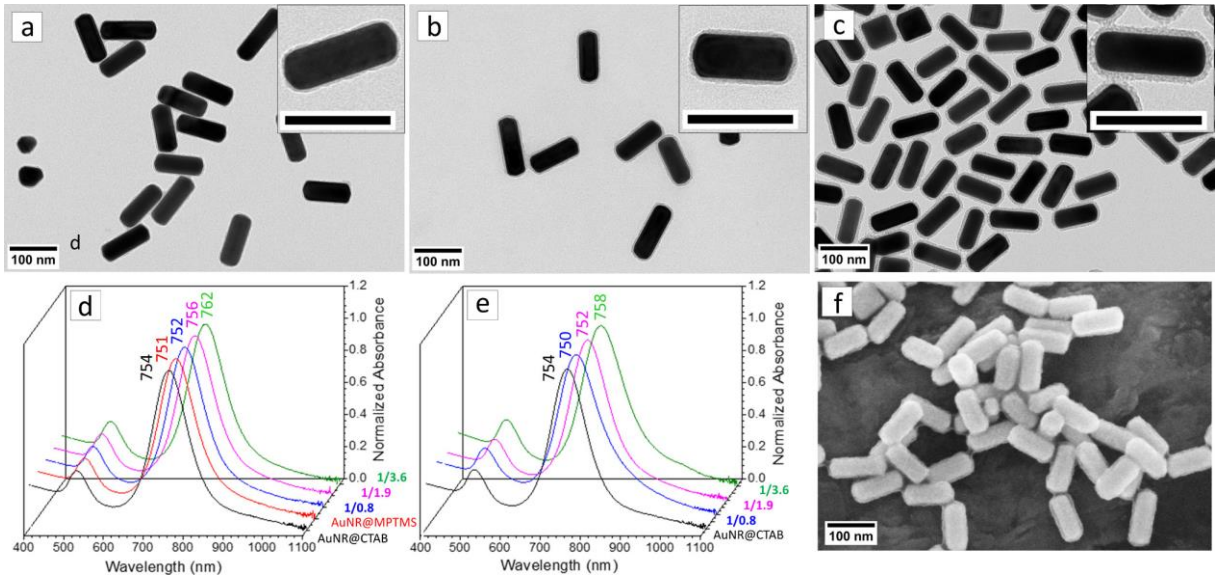

Figure 3. TEM images of AuNR@t-SiO_2 synthesized using MPTMS primer and pH monitoring with different Au/TEOS ratios: (a) 1/0.9, (b) 1/1.8, and (c) 1/3.6. Scale bars in the inset correspond to 100 nm. Extinction spectra of the obtained AuNR@t-SiO_2 (d) before purification and (e) after purification. (f) SEM image for (c).

Figure 4

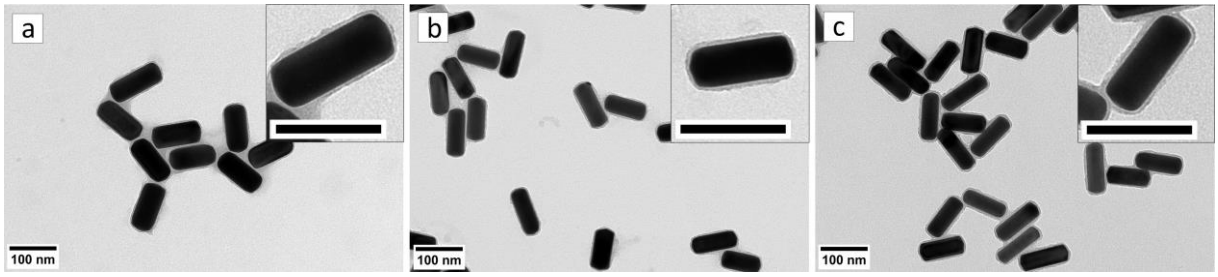

Figure 4. TEM images of AuNR@t-SiO_2 synthesized using the MPTMS primer and pH monitoring at a 1/1.8 Au/TEOS ratio with different AuNR dimensions: (a) 109 × 49 nm^2, (b) 94 × 39 nm^2, and (c) 102 × 36 nm^2.

Figure 5

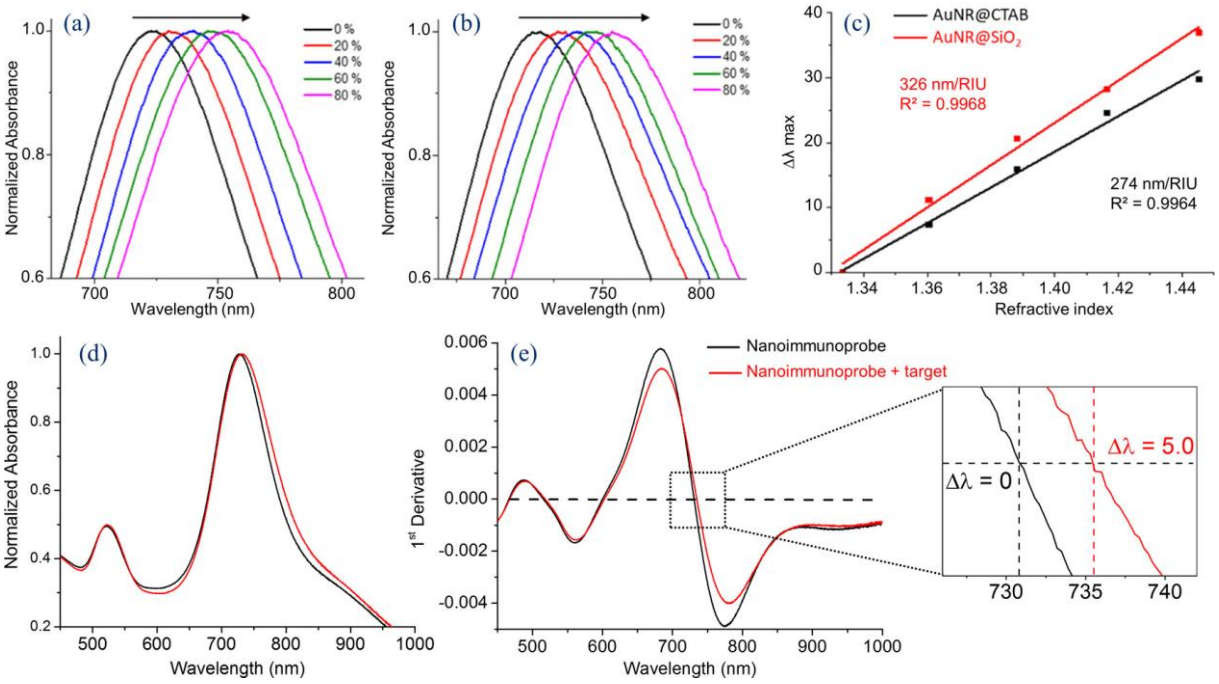

Figure 5. Normalized extinction spectra of (a) CTAB-capped AuNR and (b) AuNR@t-SiO_2 in water–glycerol mixtures of varying fractions; (c) dependence of the longitudinal plasmon shift of CTAB-capped AuNR (black squares) and AuNR@t-SiO_2 (red squares) on the refractive index of liquid mixtures. (d) Normalized extinction spectra of the nanoimmunoprobes before and after target recognition and their derivatives (e).

Table 1. Summary of the Main Characteristics of the AuNR@SiO_2 Particles Depending on the Experimental Conditions

synthesis protocol	Au/TEOS ratio	[CTAB] (mM)	reaction time	shell thickness (nm)	porosity	nucleation of SiO_2 NP	presence of SiO_2 NP after washing
(A) //m-SiO_2	1/3.6	1.1	17 days	14	// to the surface	no	no
(B) ⊥m-SiO_2	1/0.9	1.1	18 h	[a]	⊥ to the surface	no	no
	1/1.8	1.1		13		yes	yes
	1/3.6	1.1		19		yes	yes
	1/0.9	1.6	18 h	[a]	⊥ to the surface	no[b]	no
	1/1.8	1.6		17		yes	no
	1/3.6	1.6		21		yes	no
(C) t-SiO_2	1/0.9	1.6	18 h	2.1	nonporous	no[b]	no
	1/1.8	1.6		3.4		yes	no
	1/3.6	1.6		5.7		yes	no

[a]Nonhomogeneous layer.
[b][TEOS] is, in these conditions, likely to be below the critical value for homogeneous nucleation.